

# Localized-surface-plasmon-enhanced multifunction silicon nanomembrane Schottky diodes based on Au nanoparticles

Hyeon Jun Ha<sup>1</sup>, Byung Hyun Kang<sup>1</sup>, Seung-Won Yeom<sup>1</sup>, Junsu Park<sup>1</sup>, Yun-Hi Lee<sup>2,3</sup> and Byeong-Kwon Ju<sup>1,3</sup>

<sup>1</sup>Display and Nanosystem Laboratory, College of Engineering, Korea University, Seoul 136-713, Korea

<sup>2</sup>National Research Laboratory for Nano Device Physics, Department of Physics, Korea University, Seoul 136-713, Korea

E-mail: [yh-lee@korea.ac.kr](mailto:yh-lee@korea.ac.kr) and [bkju@korea.ac.kr](mailto:bkju@korea.ac.kr)

Received 23 July 2015, revised 9 September 2015

Accepted for publication 23 September 2015


Published 6 November 2015



CrossMark

## Abstract

Au nanoparticle (NP)-modified Si nanomembrane (Si NM) Schottky barrier diodes (SBDs) were fabricated by using a transfer-printing method to create pedestals using only one photomask on a flexible substrate. The transfer using the pedestals afforded a yield of >95% with no significant cracks. The plasmonic Au NPs can facilitate the improvement of the incident optical absorption. The Au NP-modified Si NM SBD exhibited enhanced photoresponse characteristics with an external quantum efficiency ( $\eta_{\text{EQE}}$ ) of 34%, a photosensitivity ( $P$ ) of 27 at a voltage bias of  $-5$  V, a light intensity of  $1.2 \text{ W cm}^{-2}$ , and a responsivity ( $R_{\text{ph}}$ ) of  $0.21 \text{ A W}^{-1}$ . Additionally, the mechanical bending characteristics of the device were observed while a compressive strain up to 0.62% was applied to the diode. The results suggest that the Au NP-modified Si NM SBD has great potential for use in multifunction devices as a strain sensor and photosensor.

 Online supplementary data available from [stacks.iop.org/NANO/26/485501/mmedia](http://stacks.iop.org/NANO/26/485501/mmedia)

Keywords: localized surface plasmon, Schottky barrier diode, silicon nanomembrane, Au nanoparticle, photosensor, strain sensor

## 1. Introduction

Localized surface plasmons (LSPs), i.e., the electromagnetic-wave-induced electrical charge density oscillations at the interface between conductive nanoparticles (NPs) that are smaller than the incident-light wavelength and the dielectric, are increasingly exploited for their potential use in several areas, including nanoscale optical and photonic devices, medical diagnostics, and sensing devices such as chemical sensors and biosensors [1–3]. The excitation of LSP resonances—particularly in plasmonic noble metal NPs such as Au, Ag, and Pt NPs placed on a semiconductor—can be used in photosensors for the enhancement of the photoresponse because of their unique optical properties such as strong optical absorption due to the trapping and scattering of incident light [2, 4, 5].

The Schottky barrier diode (SBD), comprising a semiconductor–metal contact, is one of the simplest photosensors. Schottky-type photosensors are attractive for their high speed and low-noise performance, which are attributed to the small amount of stored minority carrier charge. Si with a narrow indirect bandgap (1.12 eV) is a favorable material for the fabrication of SBDs because of its good electrical conductivity, low cost, and wide spectrum of optical absorption that corresponds to a photodetection cutoff wavelength of 1100 nm, which includes common bands in the near-infrared range (850 nm) [4, 6–8]. Since the discovery of single-crystal nanomembranes (NMs), including Si films less than a few hundred nanometers thick, Si nanomembrane (Si NMs) have been used because they have good mechanical durability and extreme flexibility and inherit the single-crystal quality and electronic properties of their bulk counterparts. These characteristics make them suitable for high-performance flexible

<sup>3</sup> Authors to whom any correspondence should be addressed.

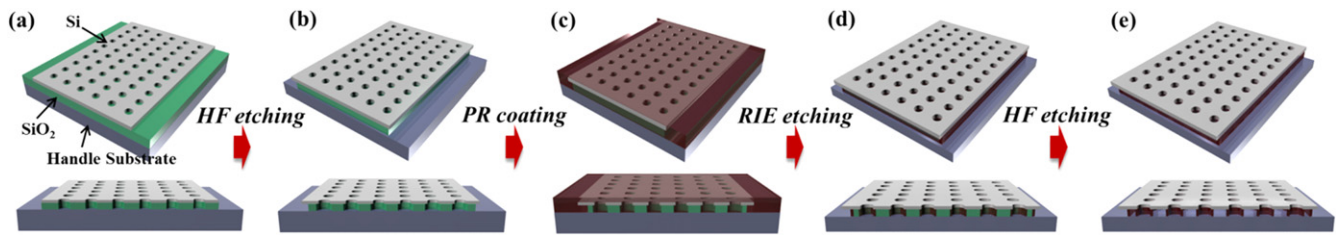


**Figure 1.** Schematic of the fabrication process for the Si NM with pedestals.

electronic/optoelectronic devices, including flexible displays, smart cards, sensors, electronic tags, and active antenna systems [9–15]. Furthermore, Si NMs on a plastic substrate have piezoresistive characteristics under strain, which can be used to create strain sensors [6, 7].

Generally, for applications in flexible devices, NMs should be transferred from handle Si using the conventional Si NM transfer method or the direct peeling-up approach [9–14]. The conventional transfer method using an elastomeric stamp and the direct transfer method are frequently accompanied by shifts, wrinkles, and cracks. To solve these problems, polymer features (i.e., pedestals) beneath the near-edge regions of the Si NM are created, which can minimize the contact area between the Si NM and the handle substrate [9, 13, 14].

In this paper, we describe the formation and properties of a Si NM SBD with Au NPs on a plastic substrate fabricated by a contact printing method using pedestals to minimize the crack occurrences. The pedestals were easily fabricated using only one photomask. This method can form top Si patterns and simultaneously cause the suspended configurations to be located not only on the edge of the Si NM but also the inside region of the Si NM, which can enhance the Si NM transfer yield by reducing the contact area between the center region of the Si NM and the handle substrate. We also propose a simple strategy to enhance the photoresponse of the Si NM SBD through the excitation of the LSP resonances in the transferred Au NPs. We examine (both theoretically and experimentally) the electrical characteristics, such as the current–voltage curves, photoresponse, optical transmittance, incident light absorbance, and mechanical bending properties of the devices. On the basis of finite-difference time-domain (FDTD) simulation results and experimental results, we ascribe the enhancement of the photoresponse characteristics to the excitation of LSP resonances through the decoration of the plasmonic Au NPs. The photoresponse and piezoresistive characteristic results suggest that Au NP-modified Si NM SBDs have potential to be used in multifunctional device applications.

## 2. Experiment

The device-fabrication process begins with the formation of microscale rectangular patterns ( $1500\ \mu\text{m} \times 1500\ \mu\text{m}$ ) with an array of holes (diameter of  $5\ \mu\text{m}$  and pitch of  $70\ \mu\text{m}$ ) on the top layer of a Si-on-insulator wafer (SoitecUnibond<sup>TM</sup>, with a p-type 100 nm Si top layer having a doping level of  $1.0\text{--}4.0 \times 10^{15}\ \text{cm}^{-3}$  and a 200 nm buried SiO<sub>2</sub> layer) by photolithography (using AZ GXR-601 photoresist (PR) and a

photomask) and reactive-ion etching (RIE) ( $\text{O}_2 = 5\ \text{sccm}$ ,  $\text{SF}_6 = 60\ \text{sccm}$ , 20 mTorr, 100 W, 39 s), as shown in figure 1(a). To fabricate the pedestals, which act as a supporting layer and a binder, the patterned samples are briefly etched in hydrofluoric acid (HF, 49%) for 1 min. The exposed buried SiO<sub>2</sub> layer between the structures and the narrow regions ( $\sim 800\ \text{nm}$ ) underneath the patterned Si layer are etched, as shown in figure 1(b). Next,  $\sim 2.5\ \mu\text{m}$  of AZ GXR-601 PR is spin-coated onto the entire sample (3000 rpm, 30 s). Simultaneously, this PR fills the exposed edges under the patterned Si, as shown in figure 1(c). The samples are hard-baked at  $95\ ^\circ\text{C}$  for 90 s. Then, oxygen plasma etching using the RIE process ( $\text{O}_2 = 20\ \text{sccm}$ , 40 mTorr, 100 W, 10 min) removes the PR everywhere, except for the region underneath the patterned Si, yielding polymeric pedestals, as shown in figure 1(d). After the pedestals are formed, the remaining 200 nm thick buried SiO<sub>2</sub> layer is completely removed by placing it in an HF bath for a few hours, as shown in figure 1(e). Using an elastomeric polydimethylsiloxane (PDMS) stamp, the released Si NM is picked up and transferred to a  $250\ \mu\text{m}$  thick polyethersulfone (PES) substrate (i-Component Co., Ltd) with the assistance of  $1.2\ \mu\text{m}$  thick SU-8 as an adhesion layer (Su-8 2002, Microchem), as shown in figures 2(a) and (c). On top of the transferred Si NM, 150 nm Au and Al metal layers are deposited (as anode and cathode, respectively) by thermal evaporation at a deposition rate of  $3\ \text{\AA}\ \text{s}^{-1}$ . Lastly, the Au NPs (British Bio Cell International, citrate-coated gold colloid 0.01% suspended in H<sub>2</sub>O) are transferred by the transfer-printing method using PDMS (similarly to the Si NM transfer-printing method), as shown in figure 2(e). Using this method, the Au NP-modified Si NM SBD is fabricated on a plastic substrate.

The  $I$ – $V$  characteristics were measured using a semiconductor parameter analyzer (Keithley SCS 4200) in a dark box (to avoid any light-induced photocurrents) at room temperature. The photoresponse of Au NP-modified Si NM SBDs and as-fabricated Si NM SBDs were characterized with different light intensities ranging from  $0.12$  to  $1.2\ \text{mW}\ \text{cm}^{-2}$  using a bottom-illuminated Xe arc lamp (150 W). The active device area receiving light was  $0.0042\ \text{cm}^2$ . A commercial FDTD software (Lumerical Solutions, Inc.) was used for the simulation. The electric-field energy distribution of the as-fabricated Si NM and the Au NP-modified Si NM was estimated. The simulation results show the profile of the electric field energy distribution at a wavelength of 520 nm, where the diameter of the Au NP was 10 nm and the thickness of the Si NM was 100 nm.

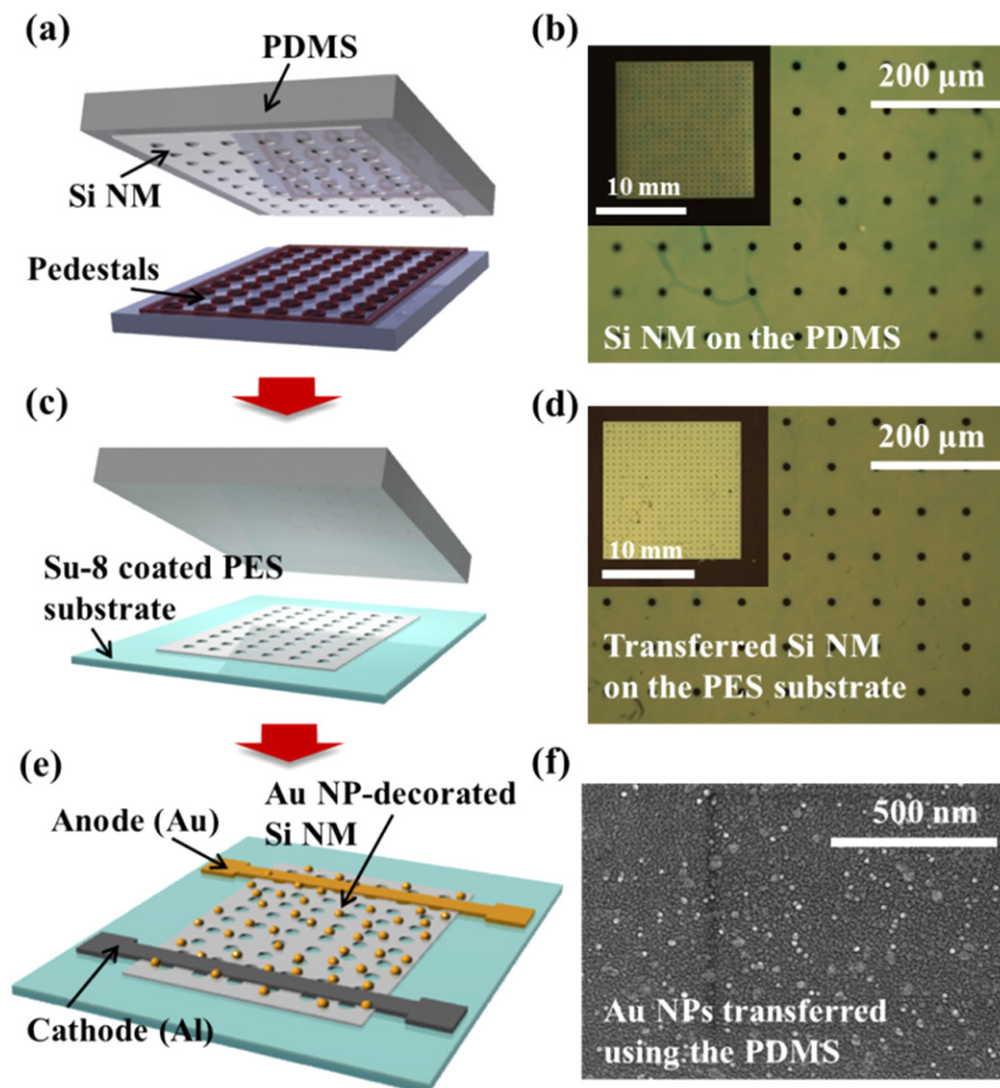


**Figure 2.** (a), (c) Process flow of Si NM transfer using the transfer-printing method with pedestals. (b), (d) Optical images of Si NMs transferred onto the PDMS stamp and the PES substrate, respectively. (e) Schematic of the Au NP-modified Si NM SBD fabricated using the transfer-printing process. (f) SEM image of the Au NPs uniformly dispersed on the transferred Si NM.

### 3. Results and discussion

#### 3.1. Characterization of Au NP-modified Si NM SBD

Figure 2(e) shows a schematic of the Au NP-modified Si NM SBD structure for a strain sensor and photosensor on a plastic substrate. This device was fabricated using a simple transfer-printing process of the Si NM with pedestals and an Au NP decoration process. Figure 2(f) shows a scanning electron microscopy (SEM) image of the Au NPs uniformly dispersed on the transferred Si NM. The average diameter and density of the Au NPs were  $10 \pm 2$  nm and  $1.2 \times 10^{10} \text{ cm}^{-2}$ , respectively. This pedestal fabrication process for the transfer printing process of the Si NMs needs only one photomask, whereas other methods need two or more patterning processes, using several photomasks for making hole-patterns to allow the etchant to penetrate. Additionally, this method can form the top silicon patterns with an array of holes and can simultaneously make the pedestal located not only the edge of

the Si NM but also the inside region, as shown in figures 2(a) and 3. Large-size Si NM needs the inside-region pedestal must minimize the contact area between the center region of the Si NM and the handle substrate, which induces strong interactions at the Si-Si interface and can easily cause cracks (as shown in figure S1 in the supporting information). Figures 2(b) and (d) show optical microscope images of the Si NMs transferred to the PDMS and the PES substrates, respectively. Using a PDMS stamp, the Si NM was picked up and transferred to a PES substrate with the assistance of SU-8 as an adhesion layer, as shown in figures 2(a) and (c). The results of this transfer-printing method indicate a yield of  $>95\%$  with no significant cracks.

Figures 3(a), (c), and (e) show SEM images of the Si NM with pedestals after the complete undercut etching of the buried SiO<sub>2</sub> layer (i.e., the fabrication process step shown in figure 1(e)). Figures 3(b), (d), and (f) present SEM images of the pedestals (width:  $\sim 800$  nm, thickness: 200 nm) remaining on the handle substrate after the Si NM was transferred onto

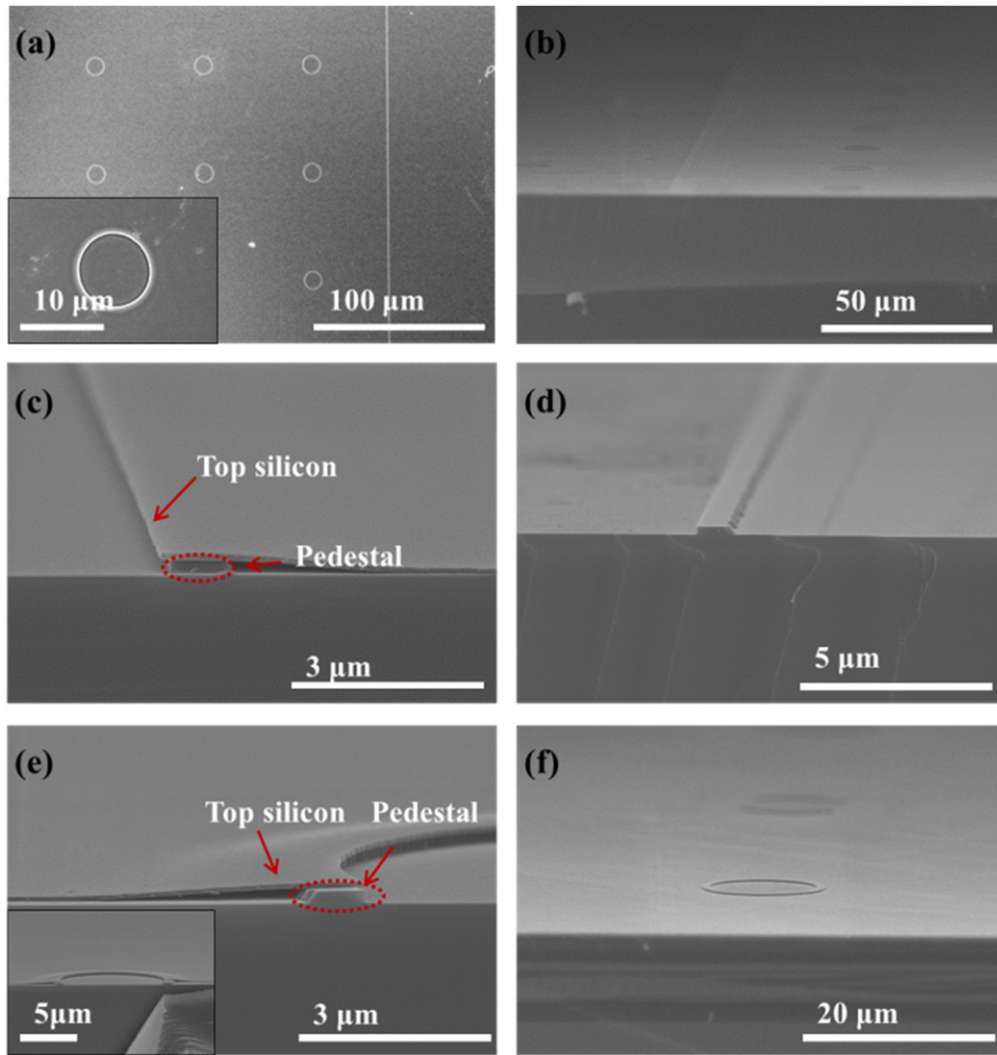


**Figure 3.** (a), (c), (e) SEM images of Si NM with pedestals after complete undercut etching of the SiO<sub>2</sub> layer. (b), (d), (f) SEM images of the remaining pedestals on the handle substrate after the Si NM was transferred onto the receiving substrate.

the receiving substrate. The widths of the pedestals depended on the etching time; their thickness was equal to that of the buried SiO<sub>2</sub> layer. These SEM images confirm that the proposed method successfully constructed pedestals underneath the hole-patterns located inside the top Si layer, which supported and bound the Si NM. The inner ring-shaped pedestals also reduced the possibility of cracks because they prevented the top Si layer from sagging by supporting and binding the Si NM.

### 3.2. Photoresponse characteristics

The forward- and reverse-bias current–voltage characteristics of the Au NP-modified Si NM SBD without light illumination were measured in a dark box (to avoid any light-induced photocurrent) at room temperature. The photoresponse measurements were conducted under illumination by a bottom-illuminated Xe arc lamp (150 W) while varying the light intensity from 0.12 to 1.2 mW cm<sup>−2</sup>, as shown in figures 4(a), 5, and 6.

The Au NP-modified Si NM SBD exhibited a clear rectifying behavior and a turn-on voltage of nearly 0 V in the dark state because of the Schottky barrier between the p-type Si NM and the Al, as shown in figure 4(a). The dark reverse current of the diode was weakly dependent on the reverse-bias voltage; it was ~0.04 mA for a reverse-bias voltage of −5 V. This Schottky barrier was also observed in the as-fabricated Si NM SBD, which exhibited similar rectifying characteristics (as shown in figure S2 in the supporting information). The current–voltage characteristics of a Schottky barrier contact are described by the following Shockley diode equation [7, 16]:

$$I = I_0[\exp(-q(V - IR)/nkT)], \quad (1)$$

$$I_0 = A^*A_{\text{eff}}T^2 \exp(-q\phi_B/kT), \quad (2)$$

where  $I_0$  is the saturation current,  $V$  is the applied voltage,  $q$  is the electronic charge,  $R$  is the series resistance,  $n$  is the ideal factor,  $k$  is the Boltzmann constant,  $T$  is the temperature,  $A_{\text{eff}}$  is the active device area,  $A^*$  is the effective Richardson constant (30 A cm<sup>−2</sup> K<sup>−2</sup> for p-type Si), and  $\phi_B$  is the barrier

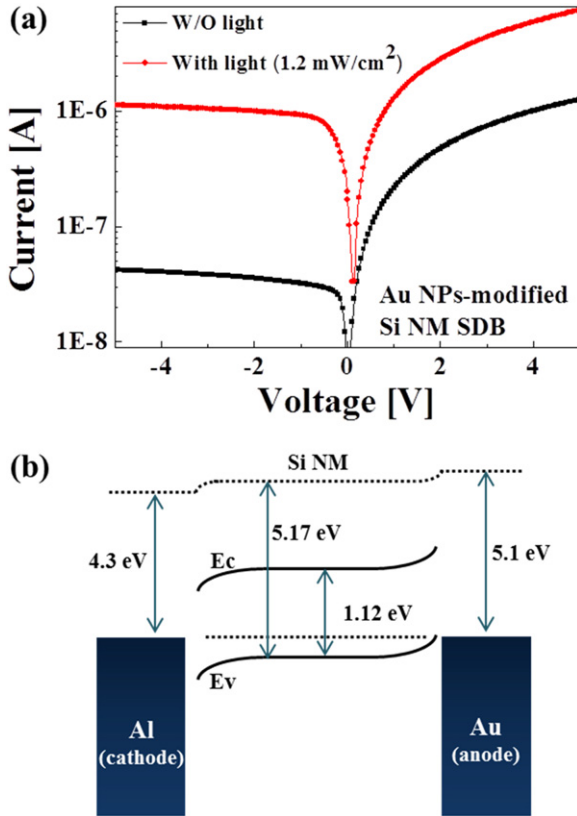


**Figure 4.** (a) Current–voltage characteristics of the Au NP-modified Si NM SBD with/without (W/O) light illumination. (b) Band diagram of the Si-metal junction; the barrier height between Al and Si was 0.68 eV.

height [6, 7]. At higher voltages, the series resistance is dominant in the diode's current–voltage characteristics. To analyze the series-resistance effect, equations (1) and (2) were rearranged in terms of the current density, as follows [7, 17]:

$$V = RA_{\text{eff}}J + n\phi_B + (nkT/q)\ln(J/A^*T^2). \quad (3)$$

To determine the series resistance and the ideality factor, equation (3) was differentiated with respect to the current density ( $J$ ). Rearranging the terms yielded the following relationship between  $d(V)/d(\ln(J))$  and  $J$ :

$$d(V)/d(\ln(J)) = RA_{\text{eff}}J + (nkT/q). \quad (4)$$

By plotting  $d(V)/d(\ln(J))$  with respect to  $J$ , the series resistance ( $R$ ) was extracted from the slope, and the ideality factor was determined according to the y-axis intercept. The calculated series resistance  $R$  was 6.3 M $\Omega$ , and the ideality factor ( $n$ ) was 1.02, indicating the high quality of the Schottky diode [6]. Using equation (2), the calculated Schottky barrier height ( $\phi_B$ ) for the Al and p-type Si contact was 0.68 eV, which closely matches that of the Al/p-type Si contact [6, 7, 18]. The large potential barrier at the interface between Al and p-type Si formed a Schottky contact, as shown in figure 4(b). The Au and p-type Si contact exhibited relatively ohmic behavior because the as-deposited Au on the p-type Si

had a lower barrier height (0.2–0.3 eV) than the Al on the p-type Si [18]. For the n-type Si, a complicated selective heavy doping process is needed to create an ohmic contact between the Si and the metal [7, 24]. During the forward-bias operation, if the Al metal is connected to a negative bias, the holes are attracted toward the Al-semiconductor interface by the forward-bias voltage. Then, the depletion region and potential barrier are reduced. Consequently, in the forward-bias region, there is a large net current. In contrast, during the reverse-bias operation, if the Al metal is connected to a positive bias, the holes are removed from the Al-semiconductor interface by the reverse bias. The depletion region and potential barrier are increased; hence, in the reverse-bias region, there is a very low net current. Under light illumination, the photo-induced current of the Au NP-modified Si NM SBD level was roughly two orders higher than the dark reverse current, and the turn on-voltage was slightly increased, as shown in figure 4(a).

As shown in figures 5 and 6, the Au NP-modified Si NM SBD and as-fabricated Si NM SBD were characterized with regard to their photoresponse. Figures 5(a) and (b) show the light-intensity-dependent photo-induced current with respect to the anode–cathode voltage of the as-fabricated Si NM SBD and the Au NP-modified Si NM SBD, respectively. Figures 5(c) and (d) show the light-intensity-dependent photo-induced current with respect to time for each device while the device was illuminated for  $\sim 10$  s for different light-intensity values (0.12, 0.36, 0.6, 0.84, and 1.2 mW cm $^{-2}$ ). The photo-induced current increased as the light intensity increased. As discussed below, because the excitation of the LSP resonance in the Au NPs increased the light absorption, the photo-induced current of the Au NP-modified Si NM SBD increased by  $\sim 24\%$  at a voltage bias of  $-5$  V under a light illumination of 1.2 mW cm $^{-2}$ , compared with the as-fabricated Si NM SBD.

The photo- and dark-current ratio and photoresponsivity are the two main factors that determine the efficiency of photodiodes. These two factors also indicate the performance enhancement of the Au NPs due to plasmonic effects in Si NM SBDs. The photosensitivity ( $P$ ) is defined according to the photo- and dark-current ratio, as follows:

$$P = (I_{\text{photo}} - I_{\text{dark}})/I_{\text{dark}}. \quad (5)$$

The responsivity ( $R_{\text{ph}}$ ) is defined as

$$R_{\text{ph}} = (I_{\text{photo}} - I_{\text{dark}})/(P_{\text{in}}A_{\text{eff}}), \quad (6)$$

where  $I_{\text{photo}}$  is the photo-induced current,  $I_{\text{dark}}$  is the dark current, and  $P_{\text{in}}$  is the power of the incident light per unit area. The responsivity ( $R_{\text{ph}}$ ) reveals the extent to which the optical power is converted to an electrical current [19]. Figures 5(e) and (f) show  $P$  and  $R_{\text{ph}}$ , respectively, with respect to the light intensity. At a light intensity of 1.2 W cm $^{-2}$  and a voltage bias of  $-5$  V, the  $P$  value of the Au NP-modified Si NM SBD was 27, and that of the as-fabricated Si NM SBD was 22. As the light intensity increased,  $P$  increased substantially, and the difference in  $P$  between the Au NP-modified Si NM SBD and the as-fabricated Si NM SBD also increased, as shown in

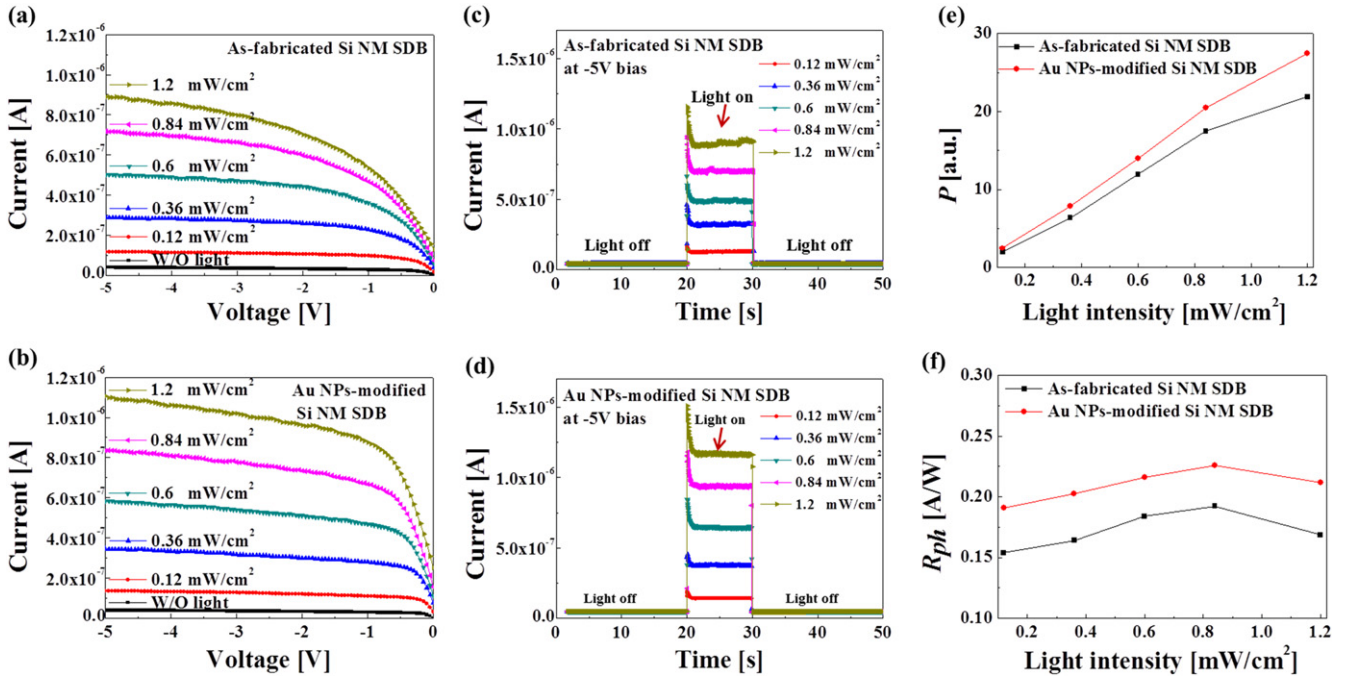


**Figure 5.** (a) Current–voltage characteristics and (c) photo-induced current change with respect to time for the as-fabricated Si NM SBD under light illumination with the light intensity increasing from 0.12 to 1.2 mW cm<sup>-2</sup>. (b), (d) Graphs for the Au NP-modified Si NM SBD. (e) Photosensitivity and (f) responsivity of the two representative diodes with respect to the light intensity.

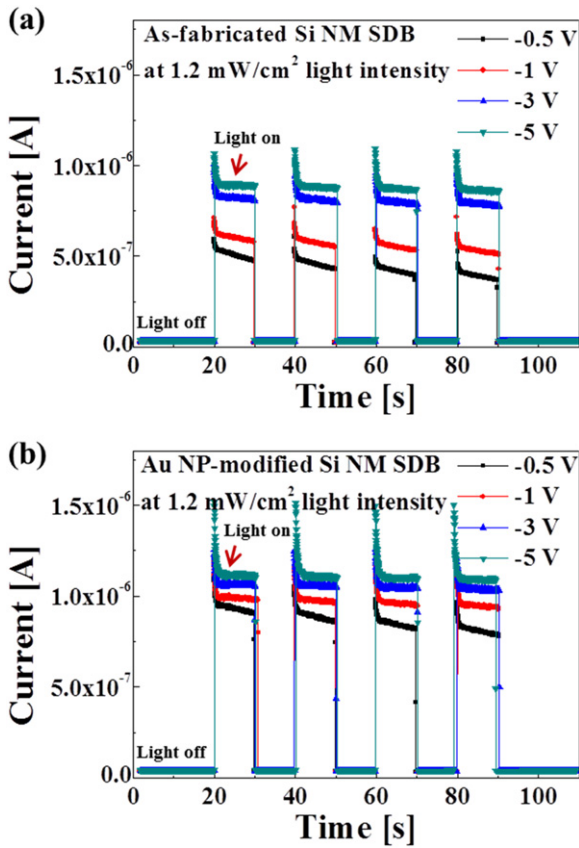


**Figure 6.** (a), (b) Photoresponse characteristics of the voltage-dependent photo-induced current versus time as the applied voltage at the anode changed from -0.5 to -5 V for the two representative diodes.

figure 5(e). The average  $R_{ph}$  was 0.21 and 0.17 A W<sup>-1</sup> for the Au NP-modified Si NM SBD and the as-fabricated Si NM SBD, respectively. The  $P$ ,  $R_{ph}$ , and photo-induced current values for the Au NP-modified Si NM SBD were higher than those for the as-fabricated Si NM SBD under the same conditions.

As shown in figure 6, we also examined the photo-response characteristics of the voltage-dependent photo-induced current with respect to time as the applied voltage at the anode was changed. Under a light illumination of 1.2 mW cm<sup>-2</sup> and 10 s on/off intervals, the photo-induced current increased with the absolute value of the applied voltage at the anode. This phenomenon occurred because of the numerous accumulated holes at the Si layer. The photo-induced current of the Au NP-modified Si NM SBD was higher than that of the as-fabricated Si NM SBD. The response for the tuning on/off time was defined as the time required for the photo-induced current to reach the  $\pm 10\%$  range of the stable state. According to figure S3 in the supporting information, the response times for turning on and off the two representative diodes were  $\sim 0.25$  s and  $< 27$  ms, respectively. The external quantum efficiency ( $\eta_{EQE}$ ) of the photodiode was calculated using the following equation:

$$\eta_{EQE} = (I_{photo}/P_{in})(h\nu/q), \quad (7)$$

where  $h$  is Planck's constant,  $\nu$  is the frequency of light in a vacuum, and  $q$  is the electron charge. The  $\eta_{EQE}$  value of the Au NP-modified Si NM SBD was 34% at a wavelength of 827 nm, which was the peak value of the Xe arc lamp. This value is  $\sim 5\%$  higher than that of the as-fabricated Si NM SBD, and the efficiency is comparable with those of previously reported photosensors [6, 20]. Table 1 presents

**Table 1.** Summary of the device performances of the Au NP-modified Si NM SBD and as-fabricated Si NM SBD.

Device	Photo-induced current (A)	Photo-sensitivity (a.u.)	Responsivity ( $\text{A W}^{-1}$ ) (average value)	$\eta_{\text{EQE}}$ (%)
Au NP-modified Si NM SBD	$1.11 \times 10^{-6}$	27	0.21	34
As-fabricated Si NM SBD	$8.89 \times 10^{-7}$	22	0.17	29

Note: At  $-5$  V voltage bias and under a light illumination of  $1.2 \text{ mW cm}^{-2}$ .

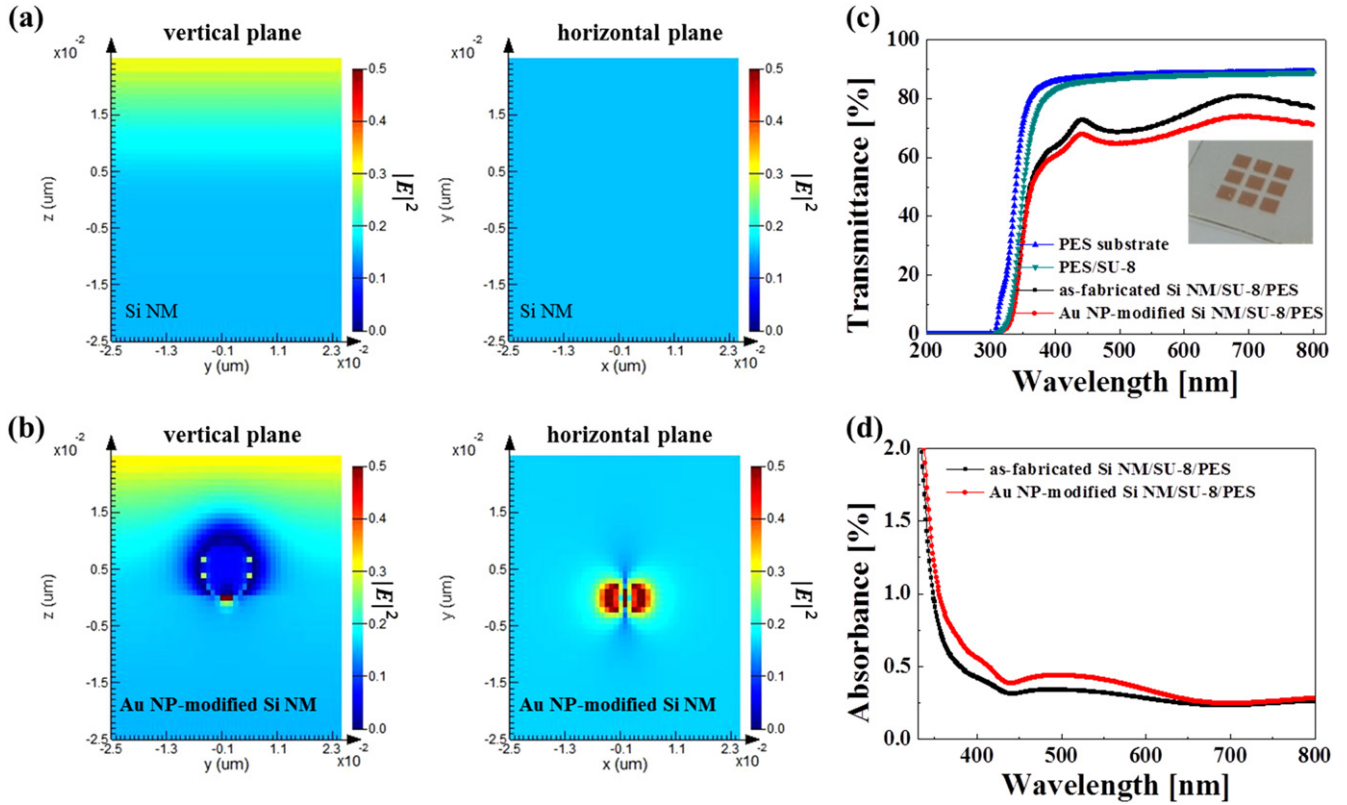


**Figure 7.** (a), (b) Simulated FDTD results for the electric-field energy distribution of the as-fabricated Si NM and Au NP-modified Si NM, respectively. (c) Transmittance spectra of a bare PES, PES/SU-8, Si NM/SU-8/PES, and Au NP-modified Si NM/SU-8/PES. Inset shows an optical image of the Au NP-modified Si NM/SU-8/PES sample, indicating its transparency. (d) Absorbance spectra of Si NMs with and without Au NP decoration.

the photo-induced current,  $P$ ,  $R_{\text{ph}}$ , and  $\eta_{\text{EQE}}$  of the Au NP-modified Si NM SBD and the as-fabricated Si NM SBD. Although the device-performance improvement was not very high, the Au NP-modified Si NM SBD exhibited a performance improvement due to the Au NP transfer-printing method using PDMS. The device performance can be further improved through the optimization of the Au NP size and density by changing the number of Au NP transfer-printing repetitions.

### 3.3. Optical simulations and characteristics

To examine the physics underlying the performance enhancement of the Au NPs, we compared the optical properties between the Au NP-modified Si NM SBD and the as-fabricated Si NM SBD using theoretical simulation tools based on the FDTD results and the fabricated devices. Figures 7(a) and (b) show the computational simulation results for the electric-field energy distribution of the as-

fabricated Si NM and the Au NP-modified Si NM, respectively [21]. Strong localized fields were observed in the coupling system composed of the plasmonic Au NPs and Si NMs. The incident light-trapping efficiency, which increased the optical absorption in the Si NM area immediately below the Au NPs, can be further enhanced by the decoration of the plasmonic Au NPs, which yields the resonant coupling of the incident light with the collective oscillation mode of the conduction electrons [1–5]. In addition, the Au NPs can act as sub-wavelength scattering elements to couple and trap freely propagating plane waves from free space into the absorbing semiconductor structure; this occurs by the forward directional scattering of the light into the Si NMs under the Au NPs. This apparent electrical-field enhancement facilitates the improvement of the electron-transport efficiency at the Si NMs under the Au NPs [3, 4]. These theoretical simulation results regarding the strong localized field due to the plasmonic Au NPs on Si NM agree well with the

transmittance and absorbance spectrum, as shown in figures 7(c) and (d). Clearly, the Au NPs increase the optical absorption of the Si NM via the light-trapping effect and the enhanced forward scattering of the incident light into the semiconductor through the excitation of the LSP resonances in the Au NPs (see figure S4 in the supporting information).

The transmittance spectrum of the Au NP-modified Si NM is shown in figure 7(c), along with the spectra for PES only, PES/SU-8, Si NM/SU-8/PES, and Au NP-modified Si NM/SU-8/PES, which are included for comparison. The rectangular-patterned thin Si NM (100 nm), including its PES substrate (250  $\mu\text{m}$ ) and the adhesive SU-8 layer (1.2  $\mu\text{m}$ ), is expected to provide a high optical transparency with an average transmittance of 73% in the visible range (400–750 nm). Using the same configuration with a Au NP decoration comprising a Si NM/SU-8/PES, an average transmittance of 68% in the visible range was measured; the Au NP-modified Si NM exhibited a high transparency. An optical image of the Au NP-modified Si NM exhibiting transparency is shown in the inset of figure 7(c). Clearly, the Au NPs increased the absorption of incident photons by the Si NM. This was also observed in the absorbance spectrum in the range of 350–700 nm, which agrees with the adsorption peak of the Au NPs (10 nm in particle size) at roughly 520 nm, as shown in figure 7(d) [5]. Moreover, the graphs of the difference in the transmittance/absorbance between the as-fabricated Si NM and the Au NP-modified Si NM agree well with the adsorption peak of the Au NPs (see figure S5 in the supporting information). Consequently, the Au NP modification is highly beneficial for the fabrication of SBDs for photosensors, as the Au NPs can provide a long optical path by light trapping and more efficient light harvesting, enhancing the light coupling efficiency between the free space and the Si NM.

### 3.4. Piezoresistive characteristics

On flexible PES substrates, the Au NP-modified Si NM SBD is mechanically flexible. The effects of mechanical bending on the characteristics of the flexible diode were characterized under different convex radii, ranging from 80 to 20 mm, as shown in figures 8(a) and (b). Figure 8(a) shows the current–voltage characteristics of the Au NP-modified Si NM SBD as a photosensor under different bending radii with a light illumination of 1.2  $\text{mW cm}^{-2}$ . The compressive strains due to bending ranges from 0.16% to 0.62% were calculated according to the following equation:  $\text{strain (\%)} = 1/[(2R/\Delta R + 1) \times 100]$ , where  $R$  is the fixture radius; and  $\Delta R$  is the thickness of the bent object, including the PES substrate (250  $\mu\text{m}$ ), SU-8 adhesive layer (1.2  $\mu\text{m}$ ), Si NM (100 nm), and Al electrode (150 nm). Under bending with a compressive strain of 0.62%, the photo-induced current increased by as much as 73% compared with the flat-state device at a voltage bias of  $-5\text{ V}$  under a light illumination of 1.2  $\text{mW cm}^{-2}$ . These results of the electrical-conductivity change are consistent with the piezoresistive behavior of p-type Si under bending tests [22, 23]. At the same bias and

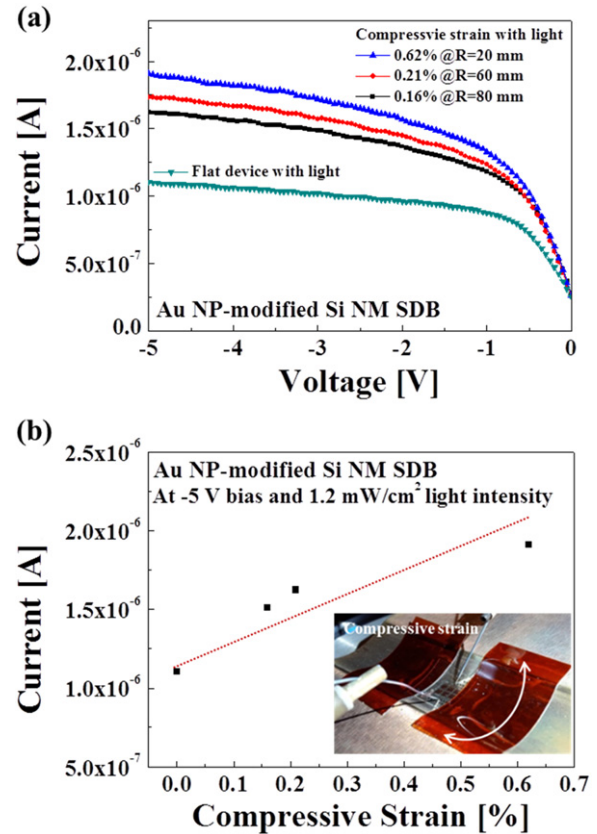


**Figure 8.** (a) Current–voltage characteristics of the Au NP-modified Si NM SBD under bending radii ranging from 80 to 20 mm (compressive strain) with light illumination. (b) Photo-induced current change with respect to the strain. Inset shows an optical image of the overall diode under a compressive strain.

wavelength, under a compressive strain, the corresponding  $\eta_{\text{EQE}}$ ,  $P$ , and  $R_{\text{ph}}$  values increased. Figure 8(b) shows the photo-induced current change (at a voltage bias of  $-5\text{ V}$ ) with respect to the compressive strain. The photo-induced current increased as the compressive strain increased. An optical image of the overall diode under a compressive strain is shown in the inset of figure 8(b). Figures S6 and S7 in the supporting information exhibit the similar current–voltage characteristics of the Au NP-modified Si NM SBD and the as-fabricated Si NM SBD, respectively, under a compressive strain without light illumination. Without light illumination, there was no difference in conductivity between the as-fabricated Si NM SBD and the Au NP-modified Si NM under compression. With light illumination, the current value of the Au NP-modified Si NM SBD was greater than that of the as-fabricated Si NM SBD diode under compression. The photo-induced current of the Au NP-modified Si NM diode increased by an average of 16% under compression with a light illumination of 1.2  $\text{mW cm}^{-2}$ , compared with the as-fabricated Si NM diode (see figure S8 in the supporting information). Therefore, only the photo-induced current of the Au NPs increased because of the enhancement of the light absorption; there was no effect on the current under compression without light illumination. Therefore, our Au NP-modified Si NM SBD can be used for sensitive flexible strain sensors under a small bending strain with or without light



**Table 2.** Summary of the device performances of the Au NP-modified Si NM SBD under a compressive strain.

Device state	Photo-induced current (A)	Photo-sensitivity (a.u.)	Responsivity (A W <sup>-1</sup> )	$\eta_{\text{EQE}}$ (%)
Flat state	$1.11 \times 10^{-6}$	27	0.21	34
Compressive strain (0.62% @ $R = 20$ mm)	$1.91 \times 10^{-6}$	35	0.37	53

Note: At  $-5$  V voltage bias and under a light illumination of  $1.2 \text{ mW cm}^{-2}$ .

illumination. Table 2 presents the photo-induced current,  $P$ ,  $R_{\text{ph}}$ , and  $\eta_{\text{EQE}}$  values for the Au NP-modified Si NM SBD under a compressive strain.

#### 4. Conclusion

A flexible Si NM SBD was fabricated with Au NP decoration on a plastic substrate using a transfer-printing method with a suspended configuration, which had a yield of  $>95\%$  with no significant cracks. The suspended configurations were fabricated using only one photomask. The proposed method can form top Si patterns and simultaneously cause the suspended configurations to be located not only on the edge but also in the inside region of the Si NM. This enhances the Si NM transfer yield by reducing the contact area between the center region of the Si NM and the handle substrate. These Au NP-modified Si NM SBDs exhibited enhancements of 24% and 5% in the photo-induced current and  $\eta_{\text{EQE}}$ , respectively, due to the plasmonic Au NPs, which facilitated the improvement of the incident-light absorption via the effective light-trapping effect and the enhanced forward scattering of incident light into the semiconductor through the LSP resonances. Additionally, these devices can be used for flexible strain sensors because of the large change in their photoresponse characteristics under a small bending strain. Therefore, the Au NP-modified Si NM SBD fabricated using a transfer method exploiting the suspended configuration has great potential for use in multifunction devices as a strain sensor and photosensor.

#### Acknowledgments

This work was supported by the Industrial Strategic Technology Development Program [10045269, Development of Soluble TFT and Pixel Formation Materials/Process Technologies for AMOLED TV] funded by MOTIE/KEIT and the KSSRC program [Stretchable Multi Sensor for Wearable IoT Device].

#### References

- [1] Lim S H, Mar W, Matheu P, Derkacs D and Yu E T 2007 Photocurrent spectroscopy of optical absorption enhancement in silicon photodiodes via scattering from surface plasmon polaritons in gold nanoparticles *J. Appl. Phys.* **101** 104309
- [2] Schaadt D M, Feng B and Yu E T 2005 Enhanced semiconductor optical absorption via surface plasmon excitation in metal nanoparticles *Appl. Phys. Lett.* **86** 063106
- [3] Lee K S and El-Sayed M A 2006 Gold and silver nanoparticles in sensing and imaging: Sensitivity of plasmon response to size, shape, and metal composition *J. Phys. Chem. B* **110** 19220–5
- [4] Luo L B, Zeng L H, Xie C, Yu Y Q, Liang F X, Wu C Y, Wang L and Hu J G 2014 Light trapping and surface plasmon enhanced high-performance NIR photodetector *Sci. Rep.—UK* **4** 03914
- [5] Wang P P, Dai W J, Ge L, Yan M, Ge S G and Yu J H 2013 Visible light photoelectrochemical sensor based on Au nanoparticles and molecularly imprinted poly(o-phenylenediamine)-modified TiO<sub>2</sub> nanotubes for specific and sensitive detection chlorpyrifos *Analyst* **138** 939–45
- [6] Oh T Y, Jeong S W, Chang S, Choi K, Ha H J and Ju B K 2013 The silicon Schottky diode on flexible substrates by transfer method *Appl. Phys. Lett.* **102** 021106
- [7] Seo J H, Oh T Y, Park J, Zhou W D, Ju B K and Ma Z Q 2013 A multifunction heterojunction formed between pentacene and a single-crystal silicon nanomembrane *Adv. Funct. Mater.* **23** 3398–403
- [8] Hsiao H T, Ni I C, Tzeng S D, Lin W F and Lin C H 2014 The n-type Ge photodetectors with gold nanoparticles deposited to enhance the responsivity *Nanoscale Res. Lett.* **9** 640
- [9] Yang Y, Hwang Y, Cho H A, Song J H, Park S J, Rogers J A and Ko H C 2011 Arrays of silicon micro/nanostructures formed in suspended configurations for deterministic assembly using flat and roller-type stamps *Small* **7** 484–91
- [10] Ying M, Bonifas A P, Lu N S, Su Y W, Li R, Cheng H Y, Ameen A, Huang Y G and Rogers J A 2012 Silicon nanomembranes for fingertip electronics *Nanotechnology* **23** 344004
- [11] Sun L, Qin G X, Seo J H, Celler G K, Zhou W D and Ma Z Q 2010 12 GHz thin-film transistors on transferrable silicon nanomembranes for high-performance flexible electronics *Small* **6** 2553–7
- [12] Xu X C et al 2014 Flexible single-crystal silicon nanomembrane photonic crystal cavity *ACS Nano* **8** 12265–71
- [13] Xu X C, Subbaraman H, Hosseini A, Lin C Y, Kwong D and Chen R T 2012 Stamp printing of silicon-nanomembrane-based photonic devices onto flexible substrates with a suspended configuration *Opt. Lett.* **37** 1020–2
- [14] Zhang K, Seo J H, Zhou W D and Ma Z Q 2012 Fast flexible electronics using transferrable silicon nanomembranes *J. Phys. D: Appl. Phys.* **45** 143001
- [15] Ha H J, Jeong S W, Oh T Y, Kim M, Choi K, Park J H and Ju B K 2013 Flexible low-voltage pentacene memory thin-film transistors with combustion-processable Al<sub>2</sub>O<sub>3</sub> gate dielectric and Au nanoparticles *J. Phys. D: Appl. Phys.* **46** 235102
- [16] Henish H K 1957 *Rectifying Semiconductor Contacts* (London: Oxford University Press)

- [17] Beadle W E, Tsai J C and Plummer R D 1985 *Quick Reference Manual for Silicon Integrated Circuit Technology* (New York: Wiley)
- [18] Cheung S K and Cheung N W 1986 Extraction of schottky diode parameters from forward current–voltage characteristics *Appl. Phys. Lett.* **49** 85–7
- [19] Kim M, Ha H J, Yun H J, You I K, Baeg K J, Kim Y H and Ju B K 2014 Flexible organic phototransistors based on a combination of printing methods *Org. Electron.* **15** 2677–84
- [20] Rochas A, Pauchard A R, Besse P A, Pantic D, Prijic Z and Popovic R S 2002 Low-noise silicon avalanche photodiodes fabricated in conventional CMOS technologies *IEEE Trans. Electron Devices* **49** 387–94
- [21] Rockstuhl C, Fahr S and Lederer F 2008 Absorption enhancement in solar cells by localized plasmon polaritons *J. Appl. Phys.* **104** 123102
- [22] He R R and Yang P D 2006 Giant piezoresistance effect in silicon nanowires *Nat. Nanotechnology* **1** 42–6
- [23] Lenkkeri J T 1986 Nonlinear effects in the piezoresistivity of P-type silicon *Phys. Status Solidi B* **136** 373–85
- [24] Smith B L and Rhoderic E H 1971 Schottky barriers on P-type silicon *Solid State Electron.* **14** 71–5